Featuring a study on machine learning-driven, self-powered wearable technology for gait-assisted healthcare by a research team led by Prof. Zong-Hong Lin from National Taiwan University, and Prof. Fu-Cheng Kao and Prof. Jen-Chung Liao from Chang Gung Memorial Hospital.

Machine learning-driven gait-assisted self-powered wearable sensing: a triboelectric nanogenerator-based advanced healthcare monitoring

Harnessing triboelectric nanogenerator technology and machine learning, a wearable insole system enables precise flat foot detection, personalized user authentication, and rehabilitation tracking—ushering in a new era of gait-assisted healthcare.

Image reproduced by permission of Zong-Hong Lin from journal, *J. Mater. Chem. A*, 2025, **13**, 13750.

As featured in:

See Jen-Chung Liao, Fu-Cheng Kao, Zong-Hong Lin *et al.*, *J. Mater. Chem. A*, 2025, **13**, 13750.

ROYAL SOCIETY OF CHEMISTRY

rsc.li/materials-a

Registered charity number: 207890

Journal of Materials Chemistry A

ROYAL SOCIETY OF CHEMISTRY

PAPER

View Article Online
View Journal | View Issue

Cite this: J. Mater. Chem. A, 2025, 13, 13750

Machine learning-driven gait-assisted self-powered wearable sensing: a triboelectric nanogenerator-based advanced healthcare monitoring†

Parag Parashar,[a] Manish Kumar Sharma,[ab] Bishal Kumar Nahak,[a] Arshad Khan,[ac] Wei-Zan Hsu,[d] Yao-Hsuan Tseng,[d] Jaba Roy Chowdhury,[a] Yu-Hui Huang,[a] Jen-Chung Liao,*[e] Fu-Cheng Kao*[ef] and Zong-Hong Lin*[a]

Advanced point-of-care healthcare systems are vital in contemporary healthcare, providing decentralized, real-time diagnostics and enabling continuous physiological assessment. Gait monitoring, a key application, benefits from wearable sensors integrated with flexible electronics, enabling precise, real-time tracking of biomechanical parameters. Despite the advantages, state-of-the-art systems are constrained by external power requirements, limited operational life, and low sensitivities, which impede their applicability. Triboelectric nanogenerators (TENGs), harnessing biomechanical motion to generate electrical signals, present a viable self-powered alternative, enhancing system autonomy and performance for real-time gait monitoring and rehabilitation. Herein, we propose a next-generation machine learning (ML)-driven TENG-based wearable sensing system for gait-assisted healthcare monitoring. The system features four TENG sensors with nylon 6/6 nanofibers and drop-like microstructured PTFE films as triboelectric layers. The sensors exhibit stable performance for 10 000 seconds, unaffected by environmental factors such as temperature and humidity. Integrated into shoe insoles at key anatomical points, they enable real-time monitoring of gait and plantar pressure distribution. By analyzing temporal variations in foot-ground contact during the gait cycle, the system accurately identifies biomechanical deviations associated with the pes planus condition, facilitating the development of prompt personalized orthotic prescriptions. Furthermore, highly sensitive TENG-based wearable sensors capture unique biomechanical signatures that can be leveraged to develop an automated, ML-driven advanced health monitoring system. First, the integration of ML algorithms enables high-precision user identification, achieving a remarkable accuracy of 99.6%. Subsequently, upon identification, personalized rehabilitation and athletic exercise programs are continuously monitored using highly accurate ML-driven systems, thereby laying a foundation for healthcare professionals to accurately assess individual recovery trajectories and optimize performance strategies. Therefore, this work represents a transformative approach to personalized healthcare, offering a self-powered, low-cost, scalable, and durable point-of-care solution for gait analysis and rehabilitation, with significant commercial potential due to its ease of use and accessibility.

Received 21st October 2024
Accepted 10th February 2025

DOI: 10.1039/d4ta07496c

rsc.li/materials-a

1. Introduction

The exponential rise in the aging population, coupled with the global health crises triggered by pandemics, has intensified the focus on point-of-care health monitoring systems.[1,2] These platforms mark a critical evolution in modern healthcare by integrating advanced wearable sensors with flexible electronics,[3] facilitating uninterrupted physiological monitoring and dynamic interaction with the human body. This enables multifaceted applications such as continuous real-time health surveillance, proactive disease diagnostics, and rehabilitation tracking, all with enhanced diagnostic accuracy, precision, and user-centric efficiency. The increasing prioritization of

[a]Department of Biomedical Engineering, National Taiwan University, Taipei 10617, Taiwan. E-mail: zhlin@ntu.edu.tw
[b]Department of Materials Science and Engineering, National Tsing Hua University, Hsinchu 30013, Taiwan
[c]International Intercollegiate PhD Program, National Tsing Hua University, Hsinchu 30013, Taiwan
[d]Institute of Biomedical Engineering, National Tsing Hua University, Hsinchu 30013, Taiwan
[e]Department of Orthopaedic Surgery, Spine Section, Chang Gung Memorial Hospital, Taoyuan 333, Taiwan
[f]College of Medicine, Chang Gung University, Taoyuan 333, Taiwan

† Electronic supplementary information (ESI) available. See DOI: https://doi.org/10.1039/d4ta07496c

personalized medicine has catalyzed significant advancements in wearable sensor technologies, resulting in devices engineered with highly specialized functionalities tailored for specific clinical applications.[4–7]

Wearable pressure sensors, including capacitive,[8,9] piezoresistive,[10,11] microfluidic,[5,12] and electromagnetic types,[13,14] have made significant strides in health monitoring. However, their reliance on external power sources, limited operational lifespans, instability, and rigid structural designs impeded their long-term applicability and performance.[15] In recent advancements, sensors based on magnetoelastic systems,[16,17] optoelectronic technologies,[18,19] and artificial intelligence[20] have emerged as promising innovations. Magnetoelastic sensors operate using external magnetic excitation fields and rely on specialized magnetostrictive materials, presenting unique operational constraints. Optoelectronic systems, while effective, are prone to risks such as damage to fibers or electronic components during use, which can limit their reliability. Artificial intelligence-based sensors, on the other hand, offer exciting potential for accurately predicting pressure values. However, this domain still demands extensive research and development to fully realize its capabilities and practical applications.

These challenges underline the need for developing self-powered, compact, flexible sensors with enhanced sensitivity, capable of operating autonomously for extended periods. Such innovations would significantly advance not only point-of-care diagnostics but also continuous health monitoring. In this context, triboelectric nanogenerators (TENGs) have emerged as a transformative technology. By coupling contact electrification with electrostatic induction, TENGs efficiently convert biomechanical energy into electrical signals,[21,22] providing a sustainable solution for wearable electronics.[15,23–29] This innovation has unlocked significant potential in medical and rehabilitation-based healthcare applications, where continuous, real-time tracking of physiological data is critical.[30,31] Applications of self-powered TENGs span a wide range of use cases, including human joint movement monitoring,[32] augmented neuromuscular transmission,[33] respiration monitoring,[34] $PM_{2.5}$ particle filtration,[35] movement tracking[36,37] and human gait analysis.[38–41] These advancements underscore the versatility and utility of TENGs in addressing key challenges in modern healthcare, particularly in enabling precise and personalized monitoring solutions.

Human gait, defined as the manner of walking, is a complex biomechanical process involving the nervous, muscular, and skeletal systems. Each individual's gait pattern is unique, acting as a biometric signature and providing crucial insights into health and mobility. Monitoring and analyzing gait patterns can reveal information about an individual's overall health, including potential neurological disorders, musculoskeletal injuries, or the effects of aging.[39,42,43] This makes gait analysis an essential tool in medical diagnostics and rehabilitation. Nonetheless, the data typically associated with human gait are highly complex, requiring significant computational resources and intricate analytical processes. Traditional methods for processing such data are often labor-intensive and time-consuming. However, the integration of artificial intelligence (AI) and machine learning (ML) technologies could revolutionize this field by automating and optimizing these tasks.[44,45] Given the complexity and variability of large gait datasets, AI and ML are crucial for enhanced accuracy and reducing the computational burden associated with traditional methods.[42,43,46] These technologies facilitate real-time data processing, enabling the detection of subtle gait anomalies that are difficult to identify manually. ML-powered models can automatically classify and analyze gait patterns, offering personalized diagnostics and intervention plans. Additionally, the Internet of Things (IoT) ecosystem enhances wearable gait monitoring systems by improving accuracy, allowing continuous monitoring, and enabling intelligent health systems for long-term care and rehabilitation.

In this work, we propose an ML-driven TENG-based low-cost, highly stable, and self-powered wearable sensing system (WSS) for gait-assisted advanced healthcare monitoring. The system is composed of an array of four TENG pressure sensors with nylon 6/6 nanofiber and microstructured polytetrafluoroethylene (PTFE) films as positive and negative triboelectric layers, respectively. The as-fabricated sensors demonstrate extended operational stability, maintaining performance for 10 000 seconds, with output unaffected by varying environmental parameters, such as temperature and humidity and gait-related factors, including frequency variations. Moreover, four highly sensitive TENG sensors have been strategically embedded within the shoe insoles at critical anatomical locations, including the heel, fourth metatarsal, first metatarsal, and big toe positions, to enable high-precision real-time human gait analysis and plantar pressure monitoring. The system leverages the temporal differences in ground contact between the heel, fourth metatarsal, first metatarsal, and big toe during the stance phase of the gait cycle to drive a time-ratio-based diagnostic model. By analyzing the sequence of these contact events, the model quantifies deviations in the biomechanical parameters of individuals with pes planus in real-time. This assessment allows for the quick prescription and modification of custom orthotics that adapt to each individual's biomechanical patterns, designed to correct the contact sequence, aligning it more closely with that of a typical healthy gait pattern. In the medical field, such models significantly improve patient outcomes by providing personalized interventions that address individual biomechanical deviations, enhancing gait efficiency, reducing discomfort, and preventing future complications.

Furthermore, leveraging the subject's biomechanical characteristics, including body mass distribution and distinct gait dynamics, an automated gait-assisted advanced healthcare monitoring system is conceptualized. Driven by ML algorithms, this platform efficiently captures and analyzes critical biomechanical parameters to enable high-precision user identification in the initial phase, achieving an accuracy of 99.6%. Subsequently, the system facilitates the continuous remote monitoring and personalized assessment of 12 rehabilitation and 13 workout exercises, tailored to each individual's prescribed therapeutic and athletic regimen. The proposed self-powered, low-cost, durable, and highly scalable TENG sensor

system represents a transformative approach for personalized healthcare, offering a point-of-care solution for gait evaluation and rehabilitation, with significant potential for commercialization due to its ease of use and accessibility.

2. Results and discussion

2.1 Design concept of the TENG-based wearable sensing system for advanced healthcare monitoring

Fig. 1a illustrates the schematic of the WSS designed for gait-assisted advanced healthcare monitoring. The TENG-based wearable sensor array (four sensors), integrated with a multi-channel data acquisition (DAQ) system, enables real-time gait monitoring through precise signal acquisition and processing. The collected signals are subsequently processed by ML algorithms, which efficiently detect and analyze key biomechanical parameters related to human gait. This integration fosters the development of an ML-driven advanced healthcare system tailored for biomedical applications, ensuring automated and enhanced patient monitoring. The simplified schematic for the ML-driven gait-assisted advanced health monitoring system (from sensing to analysis) is depicted in Fig. S1.†

The TENG sensor utilizes nylon 6/6 nanofibers and PTFE films as triboelectric contact layers and operates in a double-electrode configuration, employing aluminum (Al) as the conductive electrode. The sensor's structural composition is illustrated in Fig. 1b. The highly biocompatible PTFE film surface has been engineered with drop-like microstructures (~2 μm diameter), *via* a simple double replica molding process (Fig. S2†), to facilitate enhanced effective surface area. Analogously, the biodegradable nylon 6/6 nanofiber film (~0.155 μm diameter), fabricated through a cost-effective electrospinning technique, exhibits a high surface area-to-volume ratio.

This structural configuration enhances triboelectric charge generation by increasing the material's contact area during triboelectrification. The Scanning Electron Microscopy (SEM) images along with energy dispersive X-ray spectroscopy (EDX) mapping for the PTFE and nylon films are presented in Fig. S3 and S4,† respectively. The elemental mapping confirmed the presence of carbon (C), oxygen(O), and fluorine (F) elements in the PTFE film. Similarly, C, O, and nitrogen (N) are present in the nylon 6/6 nanofiber film. Moreover, Fourier transform infrared (FTIR) spectra of the PTFE and nylon films are depicted in Fig S5.† It could be observed that in the typical absorption spectrum of PTFE, the peaks at 1203 cm^{-1} and 1142 cm^{-1} are assigned to the asymmetric stretching vibration and symmetric stretching vibration of C–F bonds, respectively. Similarly, nylon 6,6 nanofibers are characterized by N–H stretching vibration at 3300 cm^{-1}. Other characteristic peaks for nylon 6,6 nanofiber appear around C–H stretching vibration at 2932 cm^{-1} and amide-I, amide-II, and amide-III peaks at 1639 cm^{-1}, 1537 cm^{-1}, and 1371 cm^{-1}, respectively.

The electron cloud/potential well model for charge transfer *via* contact electrification is depicted in Fig. 1c. When the nylon

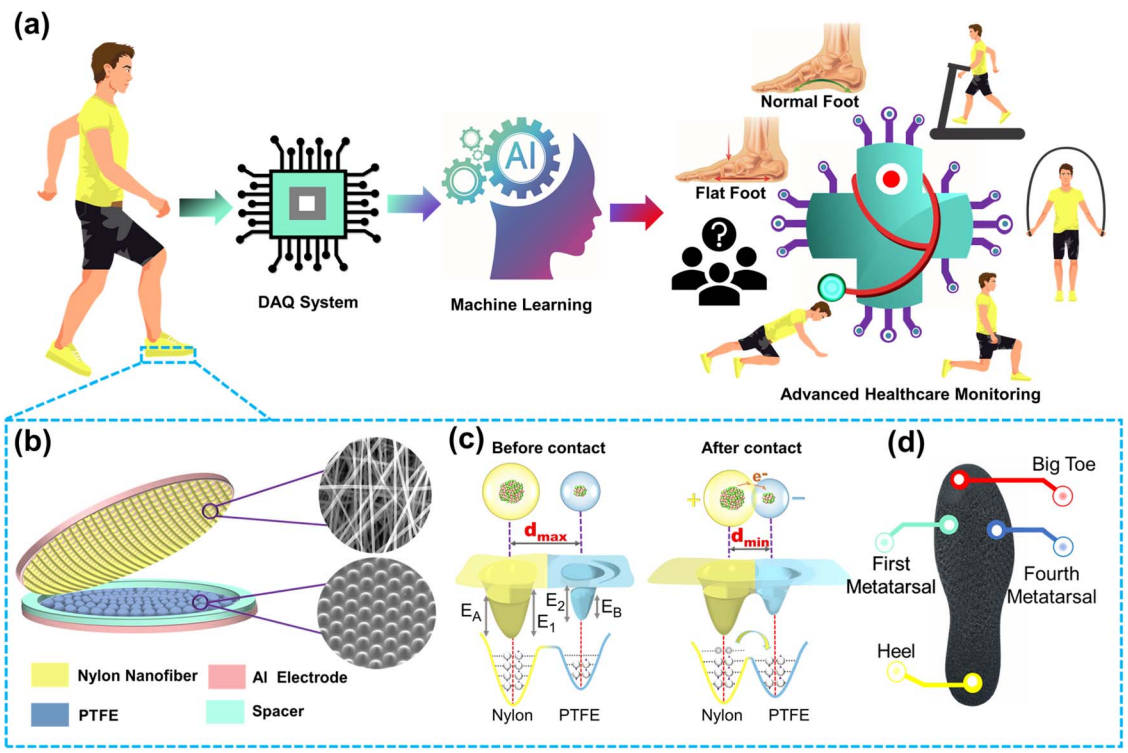

Fig. 1 Overall illustration and working kinematics of the proposed wearable sensing system-based advanced healthcare monitoring. (a) Schematic depicting the ML-driven gait-assisted healthcare monitoring concept. (b) Structure of the TENG sensor (with SEM images of the nylon nanofiber and drop-like microstructured PTFE film). (c) Electron cloud model for the charge transfer mechanism between triboelectric layers. (d) Schematic of the insole depicting TENG sensors embedded at four anatomical positions (heel, fourth metatarsal, first metatarsal, and big toe).

6/6 nanofiber and PTFE film are in a separated state, their electron clouds do not overlap, resulting in no charge transfer between the triboelectric materials. However, upon contact, the electron clouds overlap, facilitating electron transfer from the nylon 6/6 nanofiber to the PTFE film due to the lower work function of nylon 6/6, which drives the charge redistribution. Fig. 1d illustrates key anatomical positions, including the heel, fourth metatarsal, first metatarsal, and big toe regions, where the four TENG sensors have been strategically integrated into the insole structure.

2.2 Working mechanism and triboelectric capability of the TENG-based wearable sensor

The working mechanism of the self-powered TENG sensor (contact-separation mode), characterized by contact electrification and electrostatic induction phenomena, is presented in Fig. 2a. In the initial contacted state, the PTFE layer interfaces with the nylon 6/6 nanofiber membrane, resulting in the generation of negative triboelectric charges on the PTFE surface and corresponding positive charges on the nylon 6/6 substrate. In the separation state, the induced positive charges on the Al electrode facilitate a transient current flow through an external circuit, establishing charge equilibrium. In the fully separated state, the absence of external current indicates the stabilization of charge. Upon re-approaching or contact with the nylon 6/6 membrane, the sensor transitions back to the contact phase, resulting in a reverse current flow through the circuit, thereby enabling a cyclical energy harvesting mechanism. Fig. 2b presents the force response characteristics of the TENG sensor utilizing various positive triboelectric materials, specifically nylon 6/6, polyethylene terephthalate (PET), and paper, in conjunction with a common negative PTFE layer. The nylon 6/6-based TENG exhibits superior sensitivity compared to PET and paper-based TENGs across both low (0–15 N) and high (15–50 N) force regimes, demonstrating sensitivities of 19.5 mV N^{-1} and 2.93 mV N^{-1}, respectively. Consequently, in this work, nylon 6/6 has been utilized as the positive triboelectric layer to fabricate a wearable sensor with enhanced sensitivity. Furthermore, the impact of spacer thickness (Kapton tape) on force variation is illustrated in Fig. S6,† demonstrating that the configuration utilizing three layers of spacer (18 mm total thickness) achieved optimal sensitivity for the TENG sensor.

Moreover, the electric surface potentials (ϕ) of various materials, including PTFE, PVC, copper (Cu), polyvinyl alcohol (PVA), aluminum (Al), and nylon 6/6, were assessed using Kelvin

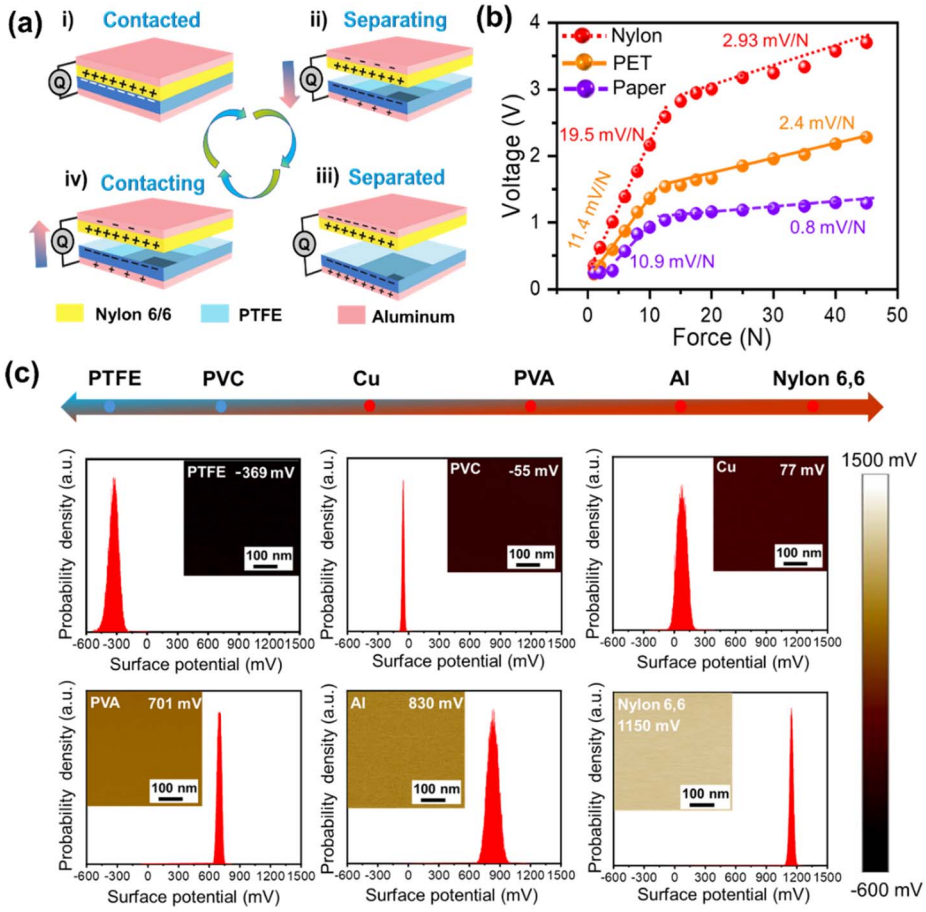

Fig. 2 Working mechanism of the TENG sensor and triboelectric series. (a) Working mechanism of the TENG (contact-separation mode). (b) Force response of the TENG sensor with various positive triboelectric materials (nylon 6/6, PET, and paper). (c) Triboelectric series of some common materials along with their surface potentials (ϕ) and Gaussian potential distributions.

Probe Force Microscopy (KPFM) under ambient conditions. Fig. 2c illustrates the relative positions of these materials within a triboelectric series alongside their surface potentials (ϕ) and Gaussian potential distributions. Notably, PTFE exhibits the most negative potential at −369 mV, indicating a strong propensity for electron acceptance. In contrast, nylon 6/6 displays the highest positive surface potential at 1150 mV, reflecting its ability to donate electrons. Therefore, charge transfer from the nylon 6/6 film to PTFE will be higher than that from other materials, which in turn will result in a higher electrical output of the TENG. In comparison, the surface potentials of PVC, Cu, PVA, and Al are at −55 mV, 77 mV, 701 mV, and 830 mV, respectively.

2.3 Electrical characterization of the TENG-based wearable sensor

The force response of the TENG-based wearable sensor from 1 N to 45 N is presented in Fig. 3a. It could be seen that as the force is increased, the voltage output of the TENG sensor also increases. The linear motor setup with the TENG sensor (top view and side view) is illustrated in Fig. S7.† Furthermore, practical wearable applications necessitate long-term stability of the sensor's output. From Fig. 3b, the fabricated sensors exhibit robust operational stability, maintaining consistent performance for 10 000 seconds. Additionally, the sensor's output remained stable for an eight-day period, thereby confirming the reproducibility of the proposed TENG sensor across multiple days (Fig. S8†). Fig. 3c and d illustrate the outputs of voltage–current density and power density, respectively, across varying external load resistances. Specifically, the voltage output increases with higher external load resistance, while the current density decreases under the same conditions. The open circuit voltage (V_{OC}), short circuit current density (J_{SC}), and maximum power density measured approximately 9 V, 0.9 mA m^{-2}, and 2.75 μW m^{-2}, respectively at an external load resistance of 70 MΩ.

The hysteresis curves shown in Fig. 3e demonstrate that the TENG-based wearable sensor exhibits remarkable hysteresis characteristics as the applied force is increased and subsequently decreased with nominal variations. As illustrated in Fig. S9,† our proposed TENG sensor demonstrated an instantaneous response time of approximately 67 ms (left inset) and a recovery time of approximately 48 ms (right inset), measured under a force of 45 N at 1 Hz frequency, indicating its suitability

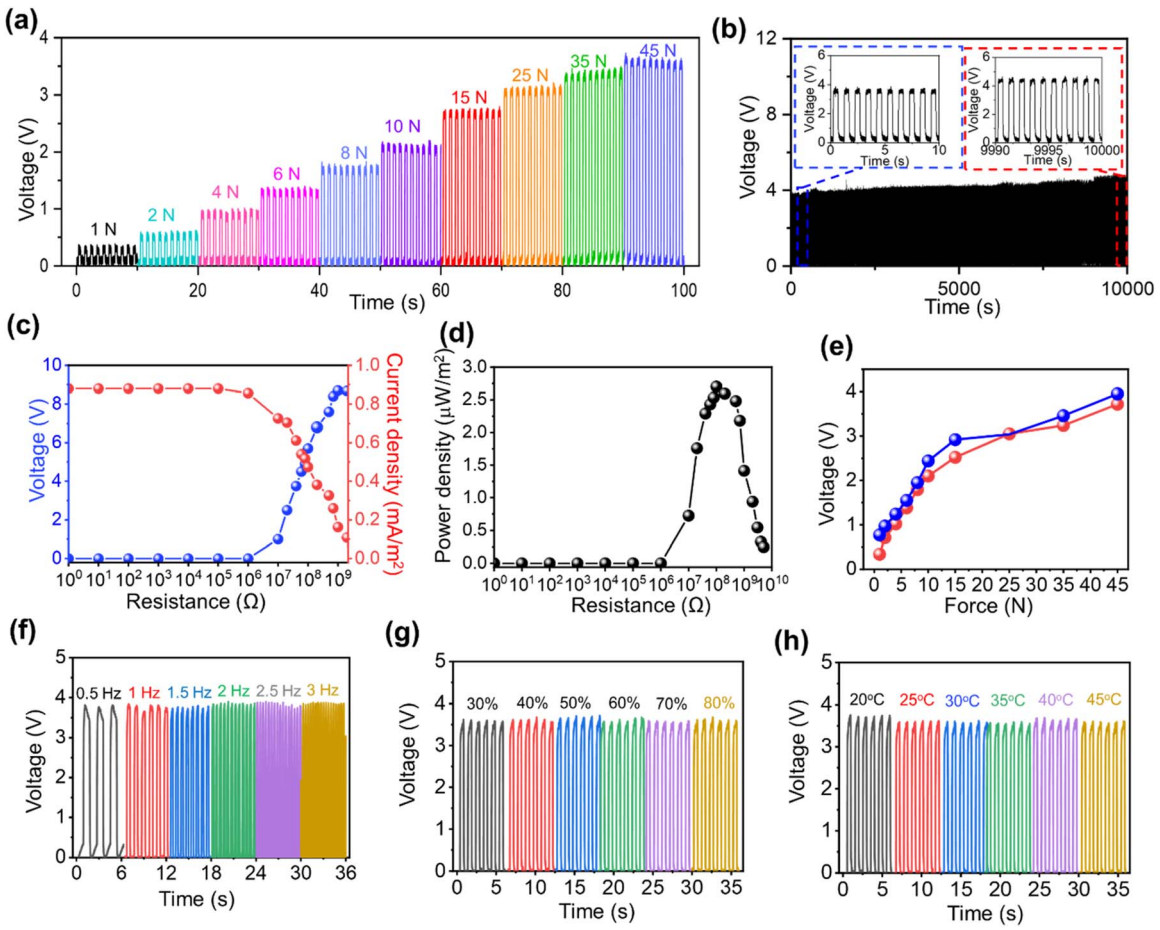

Fig. 3 Electrical characterization of the TENG sensor. (a) Force response. (b) Long-term stability (10 000 s). (c) Voltage and current density variation with resistance. (d) Power density variation with resistance. (e) Hysteresis curve. (f) TENG output response with frequency variation. (g) Humidity variation effect on TENG output. (h) Temperature variation effect on TENG output.

for real-time gait monitoring applications. Furthermore, the wearable sensor exhibited consistent electrical output when the linear motor frequency was varied between 0.5 Hz and 3 Hz, as illustrated in Fig. 3f. Additionally, we investigated the influence of diverse environmental parameters on the electrical stability of the proposed wearable sensor. The output voltage demonstrated resilience and remained unaffected by fluctuations in humidity (20–80%) (Fig. 3g) and temperature (20–45 °C) (Fig. 3h), thereby confirming the exceptional stability of the TENG-based sensor under varying environmental conditions.

2.4 Human gait cycle and real-time sensor data acquisition

Human gait refers to the biomechanical dynamics of locomotion, characterized by a repetitive sequence known as the gait cycle. This process is underpinned by the intricate coordination between afferent and efferent neural pathways, facilitating communication between the volitional control centers of the supraspinal regions and the reflexive mechanisms within the spinal cord.[47] The gait cycle encompasses two primary phases: the stance phase, wherein the reference foot (blue) maintains contact with the ground and accounts for 60% of the gait cycle, and the swing phase, comprising 40%, where the foot is elevated and moves forward,[48] as depicted in Fig. 4a. The stance phase is divided into five sub-phases: (i) initial contact (heel strike), (ii) loading response (forefoot and heel contact), (iii) mid stance, (iv) terminal stance (heel-off), and (v) pre-swing (toe-off). The swing phase includes three sub-phases, all involving the foot's elevation and forward motion. This sequence, from one heel strike to the next of the same foot, demonstrates the coordinated interaction of musculoskeletal and neuromuscular systems.

Fig. 4b depicts the dynamic response profiles of the four TENG sensors (1st, 2nd, 3rd, and 4th) under simultaneous actuation. The first curve represents the distinct electrical output generated by the 1st sensor upon initial contact. The second curve demonstrates the superimposed signal from the 1st and 2nd sensors, where the 2nd sensor is activated while the 1st

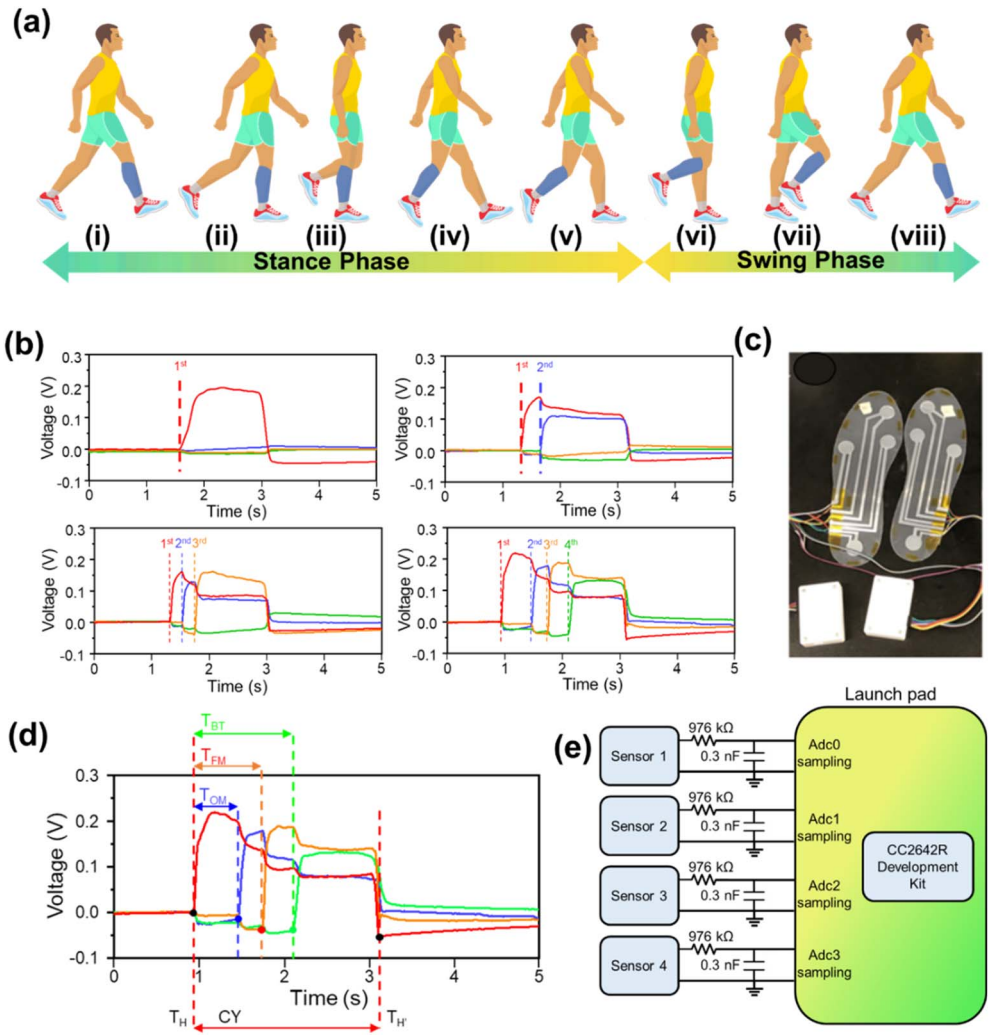

Fig. 4 Human gait cycle and real-time sensor data acquisition. (a) Typical human gait cycle-stance and swing phases. (b) Dynamic response profiles of the four TENG sensors (1st, 2nd, 3rd, and 4th) under actuation. (c) Image of the insoles with TENG sensors and DAQ. (d) Time-domain diagnostic model depiction. (e) Illustration of the CC2652R1FRGZ MCU-based DAQ system.

remains in the actuated state. Similarly, the third and fourth curves reflect the aggregate electrical responses as additional sensors (3^{rd} and 4^{th}) are consecutively triggered, resulting in cumulative output signals from multiple sensor engagements. The actual TENG sensor embedded insole image for both feet is presented in Fig. 4c. As mentioned earlier, a time-domain diagnostic model was employed for detailed gait analysis (Fig. 4d). Refer to eqn (1) and (2) for model specifics. The detailed information can be extracted from our previous work.[39]

$$\text{Time ratio} = (\text{TX} - \text{TH})/\text{CY} \quad (1)$$

$$\text{CY} = \text{TH}' - \text{TH} \quad (2)$$

The time ratio quantifies the delay between contact points during the gait cycle: TH represents the heel strike, and TFM, TOM, and TBT denote the contact instants for the first metatarsal, fourth metatarsal, and big toe, respectively. CY defines the full gait cycle duration, measured as the interval between consecutive heel strikes. By analyzing the sequence of these contact events, the model quantifies deviations in the biomechanical parameters of individuals. The DAQ system specifications are depicted in Fig. 4e. The four TENG sensors are connected to a microcontroller unit (MCU) *via* an *RC* circuit ($R =$ 976 kΩ, $C = 0.3$ nF) for signal processing. The CC2652R1FRGZ is a wireless MCU from Texas Instruments, part of the SimpleLink™ CC26xx family. The generated data are wirelessly transmitted to a human machine interface (HMI) for storage and further analysis. Real-time data acquisition and generation within the wearable sensing system for gait analysis is depicted in Movie S1.†

2.5 Application of the WSS for pes planus (flatfoot) detection, assessment, and orthotic intervention

Pes planus, commonly known as flatfoot, is marked by the collapse of the medial longitudinal arch, a valgus deformity of the heel, and medial talar prominence.[49] Factors contributing to flatfoot include ligamentous laxity, equinus deformity, tibial torsion, accessory navicular bone, congenital vertical talus, and tarsal coalition, with obesity also recognized as a contributing factor.[50] Traditional flatfoot detection methods often rely on footprint analysis, assessing the shape and pressure distribution of the foot's imprint[51] and radiographic analysis.[52] Although easy to perform and requiring minimal equipment, the footprint analysis approach lacks precision and does not provide quantitative data on the severity of the condition. In contrast, radiographic analysis offers relatively high diagnostic precision, and its limitations in visualizing soft tissue structures reduce its effectiveness for comprehensive evaluation. Furthermore, the method introduces a risk of unnecessary radiation exposure, particularly with repeated imaging, and variability in foot positioning during scans can hinder consistent identification of flatfoot deformities. Moreover, visual inspection and palpation by clinicians, while common, are subjective and depend on the examiner's experience, limiting their ability to detect subtle cases of flatfoot. These methods focus primarily on visible physical signs, offering little biomechanical insight.

In this study, we utilized a time-ratio diagnostic model that analyzes timing differences in ground contact between the heel, fourth metatarsal, first metatarsal, and big toe during the stance phase of walking. By monitoring the sequence of these contact points, the model calculates real-time deviations in biomechanical parameters in individuals with flatfoot using a time-ratio-based approach. As depicted in Fig. 5a, the schematic outlines the diagnostic process. Fig. 5b illustrates the foot of a flatfooted individual alongside orthopedic insoles. Prior to orthotic intervention, the medial aspect of the plantar surface is nearly in full contact with the ground, eliminating the foot arch and contributing to pes planus (Fig. 5c, without orthopedic insoles). When the foot bears full body weight, internal stress increases compared to those with a normal arch, potentially leading to structural deformities, degenerative changes, and complications such as osteoarthritis, plantar tendinopathy, and anterior pelvic tilt. The introduction of orthotic insoles provides structural support, emulating a natural arch and preventing the medial sole from coming into contact with the ground (Fig. 5c, with orthopedic insoles). Morphologically, these insoles redistribute plantar pressure, shifting the center of gravity laterally and creating a pressure distribution pattern similar to that of individuals with a normal arch.

Data collected for five gait cycles using the time-ratio diagnostic model (with and without orthotic insoles) reveal that, prior to the use of orthotics, the normalized time-ratio of the first metatarsal is consistently lower than that of the fourth metatarsal and big toe (TFM < TBT, TOM), as presented in Fig. 5d. This sequence reflects a foot pressure transfer pattern common in flatfoot patients: heel → inner plantar → outer plantar, leading to plantar valgus. The application of orthotic insoles reconfigures plantar pressure distribution to resemble a typical normal arch pattern (TOM < TFM < TBT): heel → lateral plantar (fourth metatarsal) → medial plantar (first metatarsal) → big toe. This adjustment improves temporal gait sequence alignment, bringing it closer to the standard healthy gait pattern (Fig. S10†). The transformation indicates that orthotic insoles effectively reduce valgus, promote the formation of an arch-like structure, and redistribute plantar pressure toward a more optimal outer-ring pattern. This enhances biomechanical alignment and improves load-bearing efficiency.

Furthermore, a ML-based classifier was incorporated to enhance diagnostic precision. This classifier, designed to evaluate key gait biomechanical parameters, achieved 100% accuracy in differentiating normal arches from pes planus (Fig. S11†). While the time-ratio diagnostic model provides biomechanical analysis and quantifies orthotic efficacy, the ML model offers robust validation, ensuring high reliability in foot type classification. Together, these systems establish a comprehensive diagnostic framework, with the time-ratio model delivering dynamic biomechanical insights and the ML model ensuring precise classification.

In summary, the time-ratio diagnostic model presents significant advantages for real-time, accurate detection and reliable assessment of flatfoot abnormalities. By analyzing

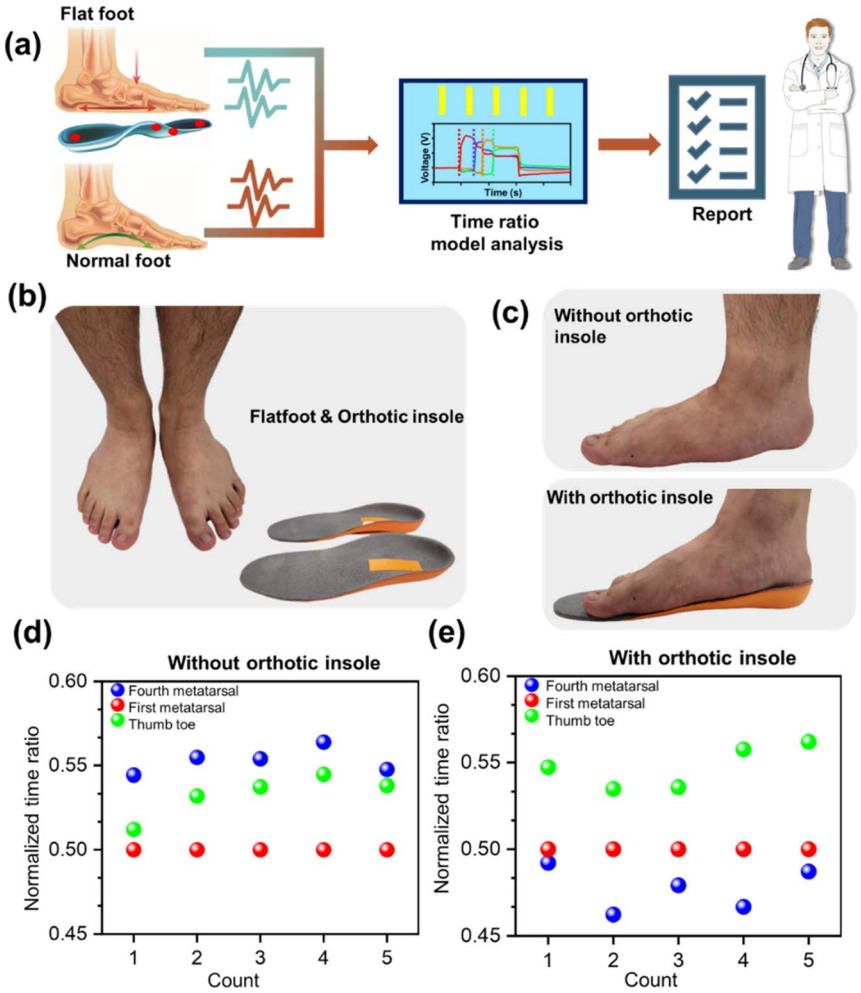

Fig. 5 Flatfoot detection, assessment, and orthotic intervention. (a) Schematic illustrating the diagnostic process. (b) Images of the flatfooted individual alongside orthopedic insoles. (c) Images representing flatfoot individual medial aspect of the plantar surface (with and without orthopedic insoles). (d) Normalized time ratio of flatfoot individuals without orthopedic insoles. (e) Normalized time ratio of flatfoot individuals with orthopedic insoles.

temporal differences in ground contact points, it enables rapid and precise identification of biomechanical deviations. Additionally, the model's ability to track dynamic plantar pressure redistribution permits real-time assessment of orthotic corrections, ensuring that clinicians can promptly modify insole designs as needed. This adaptability enhances therapeutic efficacy and allows for personalized patient care.

2.6 Application of the WSS for ML-driven gait-assisted advanced health monitoring

The asymmetrical distribution of body mass and individual gait pattern variances significantly influences the interaction dynamics and output voltage of insole sensors. Highly sensitive TENG-based wearable sensors capture unique biomechanical signatures that can be leveraged to develop an automated, ML-driven advanced health monitoring system. Real-time gait monitoring involves analyzing gait phase durations across a typical gait cycle for user identification. A conceptual model of this intelligent health monitoring framework is shown in Fig. 6a. In the initial phase, multi-channel data generated by the wearable system is acquired *via* a DAQ system, facilitating signal processing and user identification through machine learning methodologies. For simplicity, three gait phases—mid-swing (green), mid-stance (turquoise), and heel-off (pink)—are analyzed for four individuals (P1, P2, P3, and P4) under normal walking conditions (Fig. 6b).

The voltage magnitude and shape vary among individuals, indicating unique biomechanical characteristics. The extracted average durations for these gait phase events are depicted in Fig. S12.† Notably, the mid-stance phase duration exhibits the greatest variance across individuals due to differences in behavioral gait characteristics and body mass distribution, making it suitable for user identification. In addition to manual feature extraction for user identification, machine learning-assisted methods provide a lucrative alternative. The voltage signals from the four users during normal walking are processed, and the complete left foot raw data are presented in Fig. S13.† The raw data undergo standard preprocessing

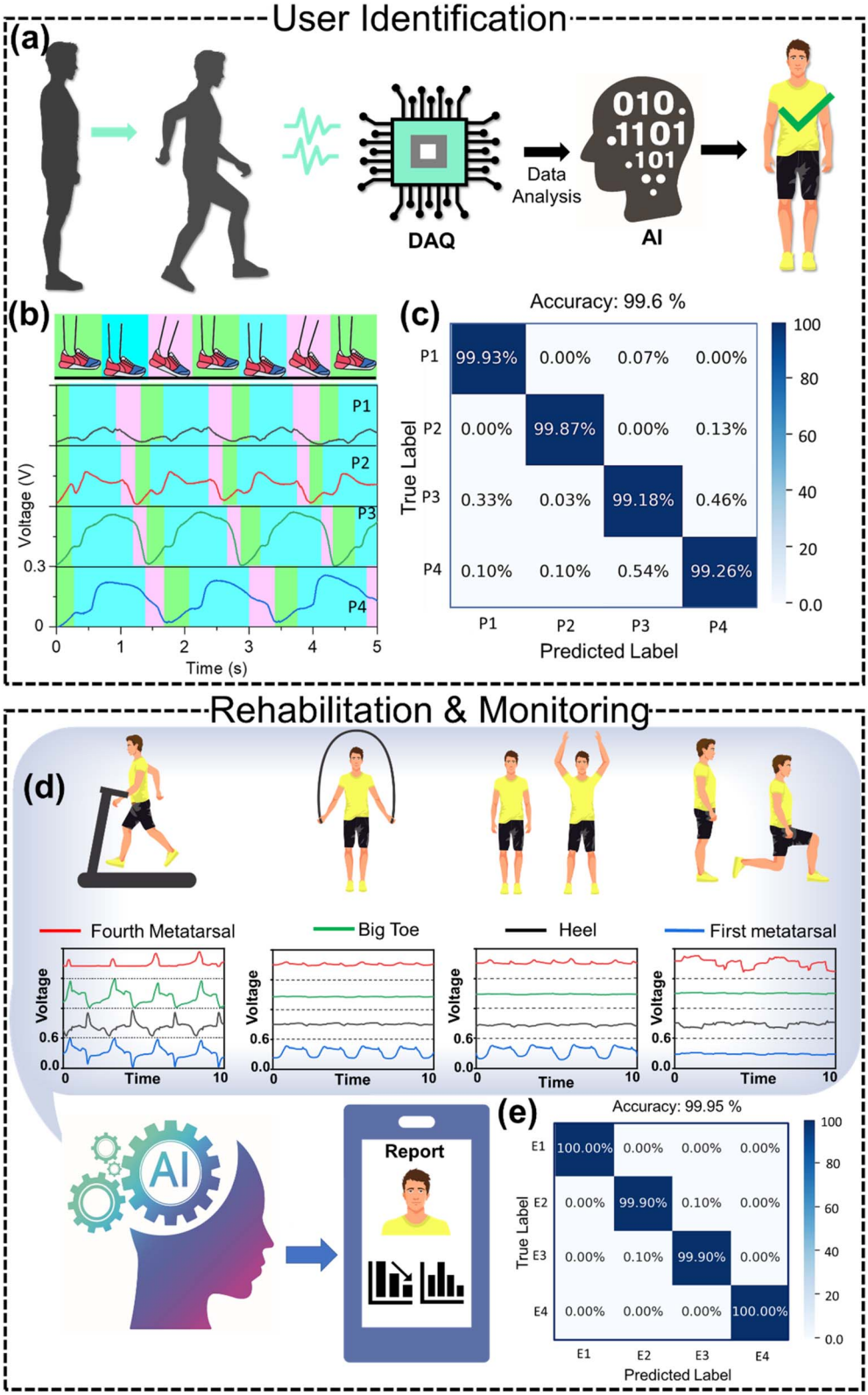

Fig. 6 Gait assisted advanced healthcare monitoring. (a) Schematic depicting initial phase-user identification. (b) Left heel data for 4 persons (P1, P2, P3, and P4). (c) User identification confusion matrix. (d) Schematic depicting second phase-rehabilitation and monitoring. (e) Confusion matrix for the classification of 4 exercises (E1, E2, E3, and E4).

techniques, including data cleansing, management of missing values and outliers, data standardization, and elimination of inconsistencies. The dataset comprises 60 000 samples (15 000 per class), with each sample containing data from the four sensors. The dataset is randomly split into an 80 : 20 ratio for training and testing. A random forest ensemble model (Fig. S14†) is trained on the training set, while the test set is utilized to evaluate model performance. The normalized multi-class confusion matrix shown in Fig. 6c indicates that the classifier achieved an overall accuracy of 99.6%. A brief description of the random forest classifier and associated dataset information for ML-assisted classifications are included in ESI Note S1.†

In the second phase, subsequent to user identification, a personalized rehabilitation plan is enacted. The user undertakes a series of exercises, each prescribed for a defined duration based on the individualized rehabilitation or athletic workout regimen (Fig. 6d). Data gathered during these exercises are subsequently processed through a ML model for analytical purposes. The unique characteristic signals produced by various exercises enable differentiation *via* ML-assisted classification. As a proof of concept, we first trained a ML model tailored specifically for only four exercises (treadmill E1, rope jumping E2, jumping jacks E3, and walking lunges E4) for an individual user, achieving an overall classification accuracy of 99.95%. The corresponding confusion matrix, which illustrates the model's performance, is presented in Fig. 6e. Furthermore, we conducted classifications across a total of 12 rehabilitation exercises (half squat, standing on tiptoes, standing on heels, lifting legs up from the front side (while standing), lifting legs up from the side direction (while standing), lifting legs up from the rear side (while standing), stepping leg up when sitting (on chair), chair-assisted tiptoe squat down and standing up, chair sitting and standing with arms akimbo, standing lunges, stepping from the side directions, and walking on heels) and achieved a remarkable accuracy of 99.96% (Fig. S15†). The associated rehabilitation exercise images and raw data (left heel) are depicted in Fig. S16 and S17,† respectively.

In addition to the rehabilitation exercises, we further classified 13 workout exercises (deep squat, mountain climbing, high knee, squat jacks, lateral lunges, rope jumping, walking up the stairs, walking down the stairs, burpees, jumping jacks, cross jumping, kicking hips, and walking lunges) with an accuracy of 99.68% (Fig. S18†). The workout exercise images and associated raw data (left heel) are presented in Fig. S19 and S20,† respectively. Analysis reveals that the data collected by our proposed WSS exhibit distinct variations, resulting in exceptionally high accuracies for ML applications. In an ideal scenario, the assessment of training efficiency, exercise completion rates, and the duration taken would occur post-training session. Such metrics are essential for healthcare professionals to gauge the patient's recovery status and can serve as a reference point for future rehabilitation or workout sessions. Thus, the integration of highly sensitive and stable TENG-based sensors into shoe insoles underscores the potential for developing an advanced health monitoring system specifically designed for point-of-care gait evaluation and sports applications.

3. Experimental section

3.1 Fabrication of microstructured PTFE layers

To begin, the mold for the microstructure was prepared by cleaning the patterned sapphire substrate with isopropyl alcohol and deionized water. A 10 : 1 ratio of polydimethylsiloxane (PDMS) and curing agent was mixed and applied to the cleaned substrate. The mixture was then evenly distributed using a spin coater at 300 rpm for 30 seconds. The coated sample was placed in a vacuum oven for 1 hour to remove air bubbles, followed by curing at 60 °C in a conventional oven for 2 hours. Once PDMS was fully cured, the layer was carefully peeled off the sapphire substrate using tweezers. This PDMS layer was subsequently used as a mold to fabricate the PTFE layer. A PTFE precursor solution was drop-cast onto the PDMS mold and heated at 120 °C for 15 minutes to evaporate the solvent. Upon curing at 120 °C, the PTFE precursor formed a microstructured PTFE film with drop-like features.

3.2 Fabrication of nylon 6/6 nanofiber membranes

Initially, a solution was prepared by mixing 10 wt% nylon 6/6 with formic acid and dichloromethane in an 8 : 2 ratio, followed by magnetization. The mixture was stirred at room temperature using a heated stirrer set to 90 rpm for 4 hours until all nylon 6/6 particles were fully dissolved. After dissolution, the mixture was transferred into a syringe connected to a syringe pump. Aluminum foil was utilized as a substrate on the collector for the electrospinning process. During the first five minutes of applying the electrical field, some fibers were collected using a slide rather than the collector and examined under a microscope to assess their morphology. The supply voltage was then fine-tuned based on the appearance of the Taylor cone at the spinneret to ensure consistent fiber production. The parameters for the electrospinning setup were configured as follows: a positive high voltage of 18–22 kV was applied, using a 21-gauge needle, with a flow rate of 0.2 mL h^{-1}, and 10 cm working distance from the needle tip to the collector. The duration of fiber collection was set at 1.5 hours. Additionally, the power supply voltage for the control slider was adjusted to 12 V, and the collector was operated at a speed of 400 rpm.

3.3 Fabrication of the TENG sensor

The developed self-powered sensor is based on a contact-mode TENG functioning as a self-powered unit. The structure utilizes a 20 mm diameter PET film as the substrate, onto which a layer of aluminum foil is adhered. The microstructured PTFE film is then attached to the aluminum foil (electrode), serving as the negative triboelectric layer. For the lower part of the structure, another 20 mm PET film is used, also layered with aluminum foil (second electrode). The nylon 6/6 nanofiber film is subsequently bonded to this aluminum layer, forming the positive triboelectric surface. Both triboelectric layers have a circular diameter of 15 mm. Adhesive tape is applied around the layers

to maintain a defined gap between the two triboelectric surfaces.

3.4 Characterization and measurements

Field emission scanning electron microscopy (FESEM) was utilized to analyze the morphological characteristics of nylon 6/6 nanofibers and microstructured PTFE films. Prior to the analysis, samples underwent an overnight vacuum treatment to eliminate moisture. Afterward, they were fixed to the sample stage with copper tape and sputtered with platinum at a current of 30 mA for 90 seconds. Scanning electron microscope (SEM) images were captured at an accelerating voltage of 10 kV. A linear motor facilitated the continuous contact-separation process to investigate charge transfer phenomena and the electrical output generated by the TENG, with data acquisition performed using a Keithley 6514 programmable electrometer. The four TENG sensors are connected to the microcontroller unit (MCU) *via* an *RC* circuit ($R = 976$ kΩ, $C = 0.3$ nF) for signal processing. The CC2652R1FRGZ MCU with wireless functionality from Texas Instruments, part of the SimpleLink™ CC26xx family, was utilized. It is designed for low-power, multi-protocol wireless communication, supporting various standards such as Zigbee, Thread, Bluetooth Low Energy (BLE), and IEEE 802.15.4. Additionally, to assess the surface potential of various materials, amplitude-modulated Kelvin probe force microscopy (AM-KPFM) was employed, specifically utilizing a BRUKER ICON system equipped with ScanAsyst technology. The detection area was maintained at 1 μm^2 in tapping mode, and to minimize tip effects, all samples were measured with the same probe tip.

3.5 Ethical approval and informed consent

All procedures performed in studies involving human participants were conducted in accordance with the ethical standards of the institutional and/or national research committee and with the 1964 Helsinki Declaration and its later amendments or comparable ethical standards. The study protocol was approved by the Institutional Review Board of the Chang Gung Medical Foundation, Taipei, Taiwan (Approval Number: 202301899B0). Informed consent was obtained from all individual participants included in the study.

4. Conclusions

In this work, we developed a machine learning (ML)-driven wearable sensing system based on TENG sensors for gait-assisted healthcare monitoring. The fabricated TENG sensor is composed of nylon 6/6 nanofibers and drop-like microstructured PTFE films as the positive and negative triboelectric layers, respectively. The fabricated sensors exhibit prolonged operational stability, maintaining consistent performance over 10 000 seconds. Their output remains unaffected by fluctuations in humidity (20–80%) and temperature (20–45 °C) levels, thereby confirming long-term stability under various environmental conditions. Additionally, the wearable sensor exhibited consistent electrical output when the frequency was varied between 0.5 Hz and 3 Hz. Four highly sensitive TENG sensors are precisely integrated into shoe insoles at key anatomical points—the heel, fourth metatarsal, first metatarsal, and big toe—allowing for high-accuracy real-time gait analysis and plantar pressure monitoring. By analyzing the sequential ground contact points, the model computes real-time deviations in biomechanical parameters for individuals with flatfoot using a time-ratio algorithm. This approach supports the integration of orthotic insoles that effectively correct valgus deformities, promoting the formation of a more anatomically normal arch structure and gait patterns by redistributing plantar pressure towards an optimized outer-ring, enhancing biomechanical alignment and load-bearing efficiency. Finally, the unique biomechanical signatures associated with human gait are exploited to develop an advanced ML-driven health monitoring system. The integration of ML algorithms enables precise user identification with an exceptional accuracy of 99.6% for 4 users. Additionally, ML-powered systems demonstrated high accuracy in classifying 12 personalized rehabilitation exercises and 13 athletic workout routines, achieving 99.96% and 99.68% accuracy, respectively. Therefore, our developed self-powered, cost-effective, flexible, and durable TENG sensor system offers an innovative solution for personalized advanced healthcare, enabling point-of-care gait evaluation and rehabilitation. Its scalability and user-friendly design make it highly suitable for commercialization.

Data availability

All data needed to evaluate the conclusions in the paper are present in the manuscript and/or the ESI file.† Additional data can be obtained from the corresponding author.

Author contributions

Parag Parashar: conceptualization, visualization, writing – original draft, writing – review & editing, software, Manish Kumar Sharma, Bishal Kumar Nahak, Arshad Khan, and Wei-Zan Hsu: methodology, data curation, formal analysis, software, Yao-Hsuan Tseng, Jaba Roy Chowdhury, and Yu-Hui Huang: data curation, investigation, formal analysis, Jen-Chung Liao and Fu-Cheng Kao: conceptualization, investigation, supervision, validation, funding acquisition, and Zong-Hong Lin: funding acquisition, conceptualization, resources, writing – review & editing, project administration, and supervision.

Conflicts of interest

There are no conflicts to declare.

Acknowledgements

This work was financially supported by the National Science and Technology Council of Taiwan (113-2636-E-002-002, 113-2628-E-002-010-MY3, 113-2640-B-002-005, 114-2923-E-002-014-MY3 and 113-2923-E-002-014-MY2), the Medical Research Project of Chang Gung Memorial Hospital (CRRPG5M0011,

CRRPG5M0012 and CRRPG3M0132) and the Ministry of Education of Taiwan.

References

1 R. Cai, C. Ngwadom, R. Saxena, J. Soman, C. Bruggeman, D. P. Hickey, R. Verduzco and C. M. Ajo-Franklin, *Nat. Commun.*, 2024, **15**, 1689.
2 S. Lee, J. S. Park, H. Woo, Y. K. Yoo, D. Lee, S. Chung, D. S. Yoon, K. B. Lee and J. H. Lee, *Nat. Commun.*, 2024, **15**, 1695.
3 H. Park, S. Kim, J. Lee, I. Lee, S. Bontapalle, Y. Na and K. Sim, *Nat. Electron.*, 2024, **7**, 39–50.
4 W. Gao, S. Emaminejad, H. Y. Y. Nyein, S. Challa, K. Chen, A. Peck, H. M. Fahad, H. Ota, H. Shiraki, D. Kiriya, D. H. Lien, G. A. Brooks, R. W. Davis and A. Javey, *Nature*, 2016, **529**, 509–514.
5 Y. Gao, H. Ota, E. W. Schaler, K. Chen, A. Zhao, W. Gao, H. M. Fahad, Y. Leng, A. Zheng, F. Xiong, C. Zhang, L. C. Tai, P. Zhao, R. S. Fearing and A. Javey, *Adv. Mater.*, 2017, **29**, 1701985.
6 J. Dunn, L. Kidzinski, R. Runge, D. Witt, J. L. Hicks, S. M. Schüssler-Fiorenza Rose, X. Li, A. Bahmani, S. L. Delp, T. Hastie and M. P. Snyder, *Nat. Med.*, 2021, **27**, 1105–1112.
7 G. Chen, X. Xiao, X. Zhao, T. Tat, M. Bick and J. Chen, *Chem. Rev.*, 2022, **122**, 3259–3291.
8 D. Yang, K. Zhao, R. Yang, S. W. Zhou, M. Chen, H. Tian and D. H. Qu, *Adv. Mater.*, 2024, **36**, 2403880.
9 F. Basarir, Y. Al Haj, F. Zou, S. De, A. Nguyen, A. Frey, I. Haider, V. Sariola and J. Vapaavuori, *Adv. Funct. Mater.*, 2024, **34**, 2403268.
10 S. Bin Choi, T. Noh, S. B. Jung and J. W. Kim, *Adv. Sci.*, 2024, **11**, 2405374.
11 S. W. Kim, J. H. Lee, H. J. Ko, S. Lee, G. Y. Bae, D. Kim, G. Lee, S. G. Lee and K. Cho, *ACS Nano*, 2024, **18**, 3151–3160.
12 T. Abbasiasl, F. Mirlou, H. Mirzajani, M. J. Bathaei, E. Istif, N. Shomalizadeh, R. E. Cebecioğlu, E. E. Özkahraman, U. C. Yener and L. Beker, *Adv. Mater.*, 2024, **36**, 2304704.
13 J. Li, S. Jia, D. Li, L. Chow, Q. Zhang, Y. Yang, X. Bai, Q. Qu, Y. Gao, Z. Li, Z. Li, R. Shi, B. Zhang, Y. Huang, X. Pan, Y. Hu, Z. Gao, J. Zhou, W. Y. Park, X. Huang, H. Chu, Z. Chen, H. Li, P. Wu, G. Zhao, K. Yao, M. Hadzipasic, J. D. Bernstock, G. M. Shankar, K. Nan, X. Yu and G. Traverso, *Nat. Commun.*, 2024, **15**, 7800.
14 J. Zhu, Y. Jia, M. Li, Z. Zhou, Y. Chen, Q. Liu and X. Yang, *npj Flexible Electron.*, 2022, **6**, 67.
15 K. Bin Chang, P. Parashar, L. C. Shen, A. R. Chen, Y. T. Huang, A. Pal, K. C. Lim, P. H. Wei, F. C. Kao, J. J. Hu and Z. H. Lin, *Nano Energy*, 2023, **111**, 108397.
16 X. Zhao, Y. Zhou, J. Xu, G. Chen, Y. Fang, T. Tat, X. Xiao, Y. Song, S. Li and J. Chen, *Nat. Commun.*, 2021, **12**, 6755.
17 Y. Zhou, X. Zhao, J. Xu, Y. Fang, G. Chen, Y. Song, S. Li and J. Chen, *Nat. Mater.*, 2021, **20**, 1670–1676.
18 Y. Chang, J. Sun, L. Dong, F. Jiao, S. Chang, Y. Wang, J. Liao, Y. Shang, W. Wu, Y. Qi and C. X. Shan, *Nano Energy*, 2022, **95**, 107061.
19 J. Sun, Y. Chang, L. Dong, K. Zhang, Q. Hua, J. Zang, Q. Chen, Y. Shang, C. Pan and C. Shan, *Nano Energy*, 2021, **86**, 106077.
20 Y. Fang, J. Xu, X. Xiao, Y. Zou, X. Zhao, Y. Zhou and J. Chen, *Adv. Mater.*, 2022, **34**, 2200252.
21 L. Jiang, X. Liu, J. Lv, G. Li, P. Yang, Y. Ma, H. Zou and Z. L. Wang, *Energy Environ. Sci.*, 2024, **17**, 3700–3738.
22 T. Zhan, H. Zou, H. Zhang, P. He, Z. Liu, J. Chen, M. He, Y. Zhang and Z. L. Wang, *Nano Energy*, 2023, **111**, 108419.
23 M. H. Kim, S. J. Park and T. J. Ha, *Energy Environ. Mater.*, 2024, **7**, e12675.
24 D. Choi, Y. Lee, Z. H. Lin, S. Cho, M. Kim, C. K. Ao, S. Soh, C. Sohn, C. K. Jeong, J. Lee, M. Lee, S. Lee, J. Ryu, P. Parashar, Y. Cho, J. Ahn, I. D. Kim, F. Jiang, P. S. Lee, G. Khandelwal, S. J. Kim, H. S. Kim, H. C. Song, M. Kim, J. Nah, W. Kim, H. G. Menge, Y. T. Park, W. Xu, J. Hao, H. Park, J. H. Lee, D. M. Lee, S. W. Kim, J. Y. Park, H. Zhang, Y. Zi, R. Guo, J. Cheng, Z. Yang, Y. Xie, S. Lee, J. Chung, I. K. Oh, J. S. Kim, T. Cheng, Q. Gao, G. Cheng, G. Gu, M. Shim, J. Jung, C. Yun, C. Zhang, G. Liu, Y. Chen, S. Kim, X. Chen, J. Hu, X. Pu, Z. H. Guo, X. Wang, J. Chen, X. Xiao, X. Xie, M. Jarin, H. Zhang, Y. C. Lai, T. He, H. Kim, I. Park, J. Ahn, N. D. Huynh, Y. Yang, Z. L. Wang, J. M. Baik and D. Choi, *ACS Nano*, 2023, **17**, 11087–11219.
25 Y. Yu, Y. Yu, H. Wu, T. Gao, Y. Zhang, J. Wu, J. Yan, J. Shi, H. Morikawa and C. Zhu, *Energy Environ. Mater.*, 2024, **7**, e12700.
26 C. Cao, Z. Li, F. Shen, Q. Zhang, Y. Gong, H. Guo, Y. Peng and Z. L. Wang, *Energy Environ. Sci.*, 2024, **17**, 885–924.
27 H. Wu, C. Shan, S. Fu, K. Li, J. Wang, S. Xu, G. Li, Q. Zhao, H. Guo and C. Hu, *Nat. Commun.*, 2024, **15**, 6558.
28 Y. Li, Y. Luo, H. Deng, S. Shi, S. Tian, H. Wu, J. Tang, C. Zhang, X. Zhang, J. W. Zha and S. Xiao, *Adv. Mater.*, 2024, 2314380.
29 T. S. Bincy, A. P. S. Prasanna, A. S. Balaji, K. J. Sivasankar, D. J. Thiruvadigal, M. Anithkumar and S. J. Kim, *Appl. Energy*, 2024, **370**, 123590.
30 T. Ahmed, Y. Gao, M. Y. So, D. Tan, J. Lu, J. Zhang, Q. Wang, X. Liu and B. Xu, *Adv. Funct. Mater.*, 2024, 2408680.
31 Y. Gai, Y. Jiang and Z. Li, *Nano Energy*, 2023, **116**, 108787.
32 A. P. S. Prasanna, V. Vivekananthan, G. Khandelwal, N. R. Alluri, N. P. M. J. Raj, M. Anithkumar and S. J. Kim, *ACS Sustain. Chem. Eng.*, 2022, **10**, 6549–6558.
33 A. P. S. Prasanna, M. Anithkumar, N. R. Alluri and S.-J. Kim, *Adv. Compos. Hybrid Mater.*, 2024, **7**, 167.
34 Y. Li, C. Liu, H. Zou, L. Che, P. Sun, J. Yan, W. Liu, Z. Xu, W. Yang, L. Dong, L. Zhao, X. Wang, G. Wang and Z. L. Wang, *Cell Rep. Phys. Sci.*, 2023, **4**, 101191.
35 X. He, H. Zou, Z. Geng, X. Wang, W. Ding, F. Hu, Y. Zi, C. Xu, S. L. Zhang, H. Yu, M. Xu, W. Zhang, C. Lu and Z. L. Wang, *Adv. Funct. Mater.*, 2018, **28**, 1805540.
36 D. Yan, D. Tao, D. Xu, Y. Sun, B. Deng, G. Cao, J. Fang and W. Xu, *Nano Energy*, 2024, **129**, 110000.
37 J. Duan, G. Yue, H. Li, T. Liu, P. Wang, W. Yu, P. Shang, C. Meng and S. Guo, *Nano Energy*, 2024, **128**, 109860.
38 L. Zhao, X. Guo, Y. Pan, S. Jia, L. Liu, W. A. Daoud, P. Poechmueller and X. Yang, *InfoMat*, 2024, **6**, e12520.

39 C. Yeh, F. C. Kao, P. H. Wei, A. Pal, K. Kaswan, Y. T. Huang, P. Parashar, H. Y. Yeh, T. W. Wang, N. Tiwari, T. T. Tsai, Y. F. Huang and Z. H. Lin, *Nano Energy*, 2022, **104**, 107852.
40 S. Hu, H. Li, W. Lu, T. Han, Y. Xu, X. Shi, Z. Peng and X. Cao, *Adv. Funct. Mater.*, 2024, **34**, 2313458.
41 Y. Wang, L. Chu, S. Meng, M. Yang, Y. Yu, X. Deng, C. Qi, T. Kong and Z. Liu, *Adv. Sci.*, 2024, **11**, 2401436.
42 C. Wei, R. Cheng, C. Ning, X. Wei, X. Peng, T. Lv, F. Sheng, K. Dong and Z. L. Wang, *Adv. Funct. Mater.*, 2023, **33**, 2303562.
43 A. Salomon, E. Gazit, P. Ginis, B. Urazalinov, H. Takoi, T. Yamaguchi, S. Goda, D. Lander, J. Lacombe, A. K. Sinha, A. Nieuwboer, L. C. Kirsch, R. Holbrook, B. Manor and J. M. Hausdorff, *Nat. Commun.*, 2024, **15**, 4853.
44 Z. Ghahramani, *Nature*, 2015, **521**, 452–459.
45 Q. Zhang, T. Jin, J. Cai, L. Xu, T. He, T. Wang, Y. Tian, L. Li, Y. Peng and C. Lee, *Adv. Sci.*, 2022, **9**, 2103694.
46 Ł. Kidziński, B. Yang, J. L. Hicks, A. Rajagopal, S. L. Delp and M. H. Schwartz, *Nat. Commun.*, 2020, **11**, 4054.
47 H. Song, T. H. Hsieh, S. H. Yeon, T. Shu, M. Nawrot, C. F. Landis, G. N. Friedman, E. A. Israel, S. Gutierrez-Arango, M. J. Carty, L. E. Freed and H. M. Herr, *Nat. Med.*, 2024, **30**, 2010–2019.
48 M. Salminen, J. Perttunen, J. Avela and A. Vehkaoja, *Gait Posture*, 2024, **111**, 1–7.
49 W. J. Noh, M. S. Lee and B. D. Lee, *Sci. Rep.*, 2024, **14**, 1–10.
50 M. Patil, M. S. Kulkarni, A. Sinha and R. R. Ghorpade, *J. Orthop.*, 2024, **57**, 90–97.
51 H. B. Menz, M. R. Fotoohabadi, E. Wee and M. J. Spink, *J. Foot Ankle Res.*, 2012, **5**, 1–7.
52 A. Stone, C. J. Stender, E. C. Whittaker, M. E. Hahn, E. Rohr, M. S. Cowley, B. J. Sangeorzan and W. R. Ledoux, *Gait Posture*, 2024, **113**, 452–461.

